

# Prospects for Direct Electron Detectors in Ultrafast Electron Scattering Experiments

Laurenz Kremeyer,<sup>1</sup> David Cai,<sup>1</sup> Malik Lahlou,<sup>1</sup> Sebastian Hammer,<sup>1,2</sup> Raphael Schwenzer,<sup>3</sup> and Bradley J. Siwick<sup>1,2</sup>

<sup>1</sup>*Department of Physics, Centre for the Physics of Materials, McGill University, Montreal, Quebec, Canada.*

<sup>2</sup>*Department of Chemistry, McGill University, Montreal, Quebec, Canada.*

<sup>3</sup>*Fachbereich Physik, Universität Konstanz, Konstanz, Germany*

(Dated: 20 February 2026)

Ultrafast electron diffraction and phonon-diffuse scattering (UED(S)) experiments make use of photo-induced changes to electron scattering intensity across 2D detectors to report on a very wide range of dynamic structural phenomena in molecules and materials. Compared to ultrafast spectroscopies, these techniques have very high structural-information content and competitive time-resolution, but sensitivity to relative changes in electron scattering intensity is orders of magnitude lower. Hybrid pixel counting detectors (HPCDs) are a promising technology for improved sensitivity and signal-to-noise in UED(S) experiments, as they offer near-zero readout noise and dark counts with the possibility of new acquisition modalities (e.g. shot-to-shot normalization) due to their high frame rates. However, it is well known that HPCDs suffer from count losses at high electron fluxes even in CW beam applications. How this translates to ultrashort electron pulse exposures has yet to be determined and is critical to understanding the application of this technology to ultrafast electron scattering experiments. Here we show that count losses are exacerbated significantly in ultrafast (pulsed) experiments and that HPCDs require count rates to be kept below  $\approx 2$  electrons per pixel per pulse. This count-rate limitation presents a severe constraint on electron bunch charge when interrogating single crystal samples. A model for the electron counting uncertainties in HPCDs across the entire relevant range of average count rates is proposed, from which we derive experimental strategies to optimize data quality in UEDS using direct electron detectors. Finally, we suggest ways HPCDs could be better adapted to ultrashort pulsed beam experiments.

## I. INTRODUCTION

Ultrafast laser-pump, electron (or X-ray) probe experiments have made it possible to directly measure structural and electronic dynamics in molecules and materials in the time-domain<sup>1,2</sup> with sub-50 fs resolution. These nonequilibrium methods provide access to many of the microscopic processes that underlie material properties, including electron-phonon<sup>3–5</sup> and phonon-phonon coupling<sup>6,7</sup>, lattice, charge and orbital ordering phenomena<sup>8–10</sup>. The ability to interrogate photo-induced phase transitions with these techniques has also deepened our understanding of how to optically prepare and control novel states of materials that exhibit properties that are inaccessible under equilibrium conditions<sup>11–13</sup>.

Here we focus on ultrafast electron-probe experiments. The default mode of data acquisition in these experiments is time-resolved scattering (Fig. 1), with the scattering signals measured over a range of scattering-angles using a 2D detector. Although time-resolved transmission electron imaging/microscopy is also under active development<sup>14</sup>, we will not discuss the particularities of time-resolved image resolution and sensitivity (detector quantum efficiency), focusing entirely on electron scattering measurements. An essential feature of the raw scattering signals measured is that they can be distributed highly non-uniformly across the detector. For gas-phase samples, polycrystalline materials or textured films, the dynamic range of the raw scattering signals tends to be narrow. For example, in a pattern of polycrystalline monoclinic VO<sub>2</sub>, the dynamic range between low- versus high-index Debye-Scherrer ring intensities measured under typical conditions in an ultrafast electron diffractometer is only of or-

der  $\approx 10$ . When probing high-quality single crystal samples, however, scattering is concentrated into Bragg peaks and the dynamic range of the raw scattered intensity tends to be many orders of magnitude larger than that observed from polycrystalline, amorphous or gas-phase samples. For example, under typical experimental conditions peak intensity in the first and second order Bragg reflections of graphite is  $10^5$  times the intensity of the phonon diffuse scattering features observable between the Bragg peaks<sup>15</sup> (Fig. 1).

The relevant signals in UES are the pump-probe delay-time dependent changes in electron scattering that result from photoexcitation of the sample, measured over as wide a range of scattering vector as possible. Current state of the art measurements are capable of resolving differential scattering signals (i.e. pump-on minus pump-off) at the 1–10% level relative to the unpumped scattering intensity, although signals approaching 0.1% have been reported for high-intensity features (Bragg peaks). To achieve a SNR (signal-to-noise ratio) of 5 for a signal change of 1%, differential scattering intensity measurements with a relative uncertainty (or relative standard error of the mean) of 0.002 are required. If the measurement is shot-noise limited, this requires the feature in question to contain at least 240,000 counts.

It is worthwhile to compare these actually measured signals with those that can be expected under weak-excitation conditions in a system that does not undergo a structural phase transition. For example, if laser-deposited energy results a 10 K increase in specimen temperature (after full thermalization) the (200), (300) and (400) Bragg peaks in graphite would be suppressed by 0.05%, 0.16% and 0.25% respectively (at room temperature) while single phonon diffuse scatter-

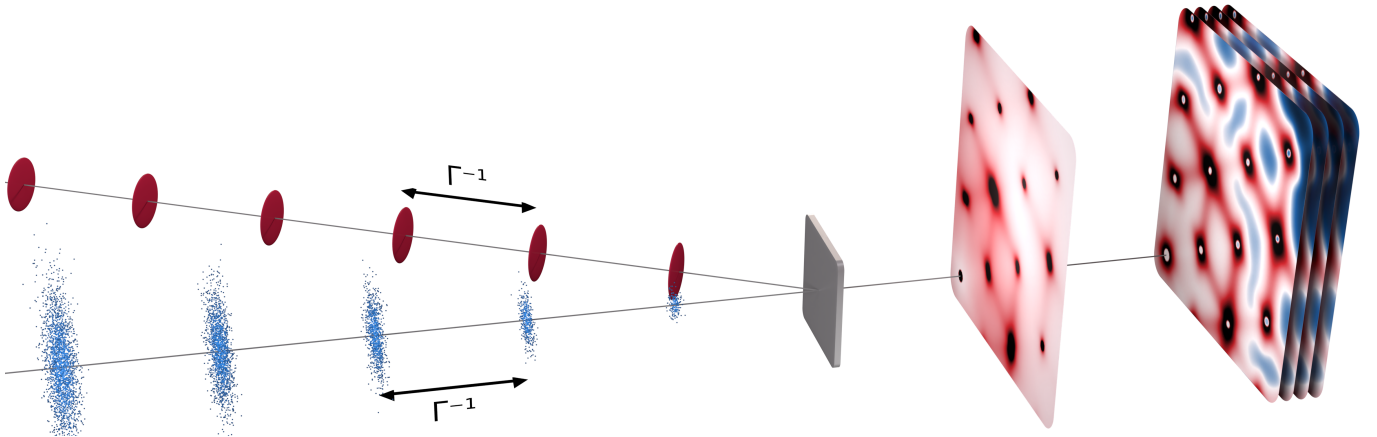


FIG. 1. Schematic illustration of the experimental setup. Electron bunches (blue particle clouds) are compressed and focused onto the sample in normal incidence and produce a diffraction pattern on the detector, represented by a plane behind the sample. Simultaneously, the sample can be illuminated with a short optical laser pulse (red discs) with an adjustable time-delay. The temporal distance between electron bunches and optical pulses is dictated by the laser amplifier, in our case  $\Gamma^{-1} = 1$  ms. The four screens on the far right side illustrate how difference images are calculated for different delay times. Red (blue) regions increase (decrease) in diffracted intensity. Projected onto the screen are simulated diffraction patterns of graphite.

ing from low-frequency acoustic modes increases by approximately 3% and optical modes by only 0.1–0.3%. Measurements of signal changes at the 0.1% level (or even the 0.001% level) are required to access the weak pump-excitation regime in UED(S) experiments. Under shot-noise limits, every 10-fold improvement in the resolvable relative signal change (at constant SNR) requires a 100-fold increase in the number of counts contained in the feature measured. Thus, a critical direction for improving the sensitivity of UED(S) measurements has been maximizing electron count rates and the primary argument favouring the development of high bunch charge and high repetition rate ultrafast electron sources<sup>1,16</sup>. However, stretching the dynamic range of detectors at both high and low count rates is also essential to enhance sensitivity, providing a strong argument in favour of improved detector technology. The detector noise-floor, specifically, is the essential determining factor for low electron count rate UED(S) signals to be reliably measured (or measured at all). HPCDs<sup>17</sup> operating in electron counting mode reduce readout and dark noise to near-zero which may open the possibility of shot-noise limited measurements even at the extremely low count rates associated with phonon-diffuse scattering signals in UED(S) measurements and other low scattering cross section inelastic processes in the nascent technique of ultrafast electron energy loss spectroscopy (uEELS)<sup>18,19</sup>.

Here we report on the performance of HPCDs, specifically the Dectris Quadro, in ultrafast electron scattering experiments. Being true electron-counting detectors, HPCDs have a number of potential signal-to-noise advantages over other technologies in use (Microchannel plate and Phosphor scintillator-based detectors) that could lead to improved sensitivity in UED(S) experiments. Sensitivity in UES currently lags far behind that of ultrafast spectroscopy and improvements in this area could significantly broaden the scope of this technique, particularly in the direction of weaker-excitation levels.

In this article we discuss the mechanisms and statistics of electron counting detectors for ultrafast electron diffraction in depth, revealing their limitations in ultrafast applications and presenting strategies to optimize SNRs using HPCDs. Throughout, we express the electron dose received by the detector in terms of electrons/pulse per pixel (EPP),  $\bar{\lambda}$ . In current instruments, the electron dose can range from many thousands in the main beam to tens in the brightest Bragg peaks of a diffraction pattern to arbitrarily small values in the diffuse features between Bragg peaks. One can convert the electron dose from a per-pulse basis to a per-time basis by simply multiplying the electron dose in EPP by the laser repetition rate  $\Gamma$ .

The remainder of this paper is organized as follows. In Section II, we describe the ultrafast electron source and detector used in this our study. In Section III A, we investigate the counting behaviour of the detector at the single detector pixel level in response to average count rates ranging from 0.16 to 7.6 EPP in two different modes of operation. In Section III B we investigate the determinants of measurement uncertainty in unpumped single-shot polycrystalline monoclinic VO<sub>2</sub> diffraction patterns over a range of EPP conditions between  $10^{-3}$  and 3, establishing a cross-over from shot-noise limited performance to count-saturation limited performance around 1 EPP, and present a quantitative model for this behaviour. In Section III C, we characterize the full experimental noise spectrum in recorded polycrystalline Pt UED patterns, and investigate the influence of the diffraction image normalization period (from shot-to-shot to time-averaged) on the SNR of pump-probe UED signals. Finally, we conduct pump-probe experiments on polycrystalline VO<sub>2</sub> with count rates between 0.5 and 1.8 EPP to validate our model for experimental uncertainties in UED using an HPCD.

## II. METHODS

The key features of the experimental setup used to determine Dectris Quadro performance in UED(S) applications are described below, focusing on the properties of the electron source and detector.

### A. Hybrid Pixel Counting Detector

All hybrid pixel counting detectors (HPCD) in use have two main components, which are bump bonded together: (i) a high-resistivity semiconductor layer with a pixelated pn-diode structure and (ii) a readout ASIC (application-specific integrated circuit) array<sup>20</sup>. The Dectris Quadro has  $512 \times 512$  pixels, each  $75 \times 75 \mu\text{m}^2$ . Incident electrons (or X-rays) deposit energy into a pixel in the sensor layer, creating electron-hole pairs. An applied bias voltage across the layer collects those charges and results in a small current. Every pixel has its own amplification, discrimination, and counting circuit, dramatically improving readout noise and dark current in recorded images<sup>21</sup>. An electron count is registered when the signal level generated by a pixel rises above a threshold value. This threshold can be set at different levels in software depending on the incident electron energy. A fundamental drawback of the counting electronics is the dead-time following the registration of ‘a count’ (100 ns for the Dectris Quadro), during which additional counts cannot be registered. Thus,  $1/\text{dead-time}$  sets the nominal maximum count rate that can be registered per pixel in CW beam applications (1,107 EPP). However, the Quadro detector (and other HPCD detectors) features a so-called *instant retrigger* mode designed to improve high-rate counting by measuring the *time above-threshold* for the pixel signal, which correlates with the number of electrons hitting the pixel inside the deadtime window<sup>22</sup>. This provides a means to reduce count losses from pulse pile-up in CW applications. Here we test the retrigger mode for ultrafast pulsed exposures and demonstrate that it is ineffective at reducing pulse pile-up related count losses under these conditions and introduces noise to the counting.

### B. Electron Source

The Radio-Frequency (RF) compressed ultrafast electron scattering instrument used in these studies operates at 90 keV electron beam energy and is described in further detail elsewhere<sup>23,24</sup>. Electron pulses containing anywhere from 0 to  $10^7$  electrons can be generated up to a maximum pulse repetition rate of 1 kHz (laser-limited) via photoexcitation of a solid copper photocathode with 260 nm UV pulses (4.77 eV photon energy). The UV pulses are generated by third harmonic generation from a 1 kHz Ti:Sapphire chirped pulse amplified laser seeded by a frequency-doubled Erbium Fiber Laser. At the detector these electron pulses are  $< 10$  ps in duration, approximately 4 orders of magnitude shorter than the deadtime, resulting in an effectively instantaneous exposure from the

perspective of the readout electronics. Ultrafast exposure conditions represent the worst-case scenario from the perspective of pulse pile-up when multiple electrons hit a pixel inside a single shot. The time between pulses (1 ms) by contrast is 4 orders of magnitude longer than the dead-time, which means that pulse pile-up is not a concern between shots up to repetition rates of 1 MHz.

The Quadro has a triggerable maximum full-frame 16-bit readout rate of 2250 Hz<sup>20</sup> that is more than sufficient to acquire the images produced by single electron pulse exposures at the maximum repetition rate of our experiments. Single-shot images are essential for testing the counting behaviour of the HPCD pixels in all readout modes during ultrafast exposures over a range of electron dose conditions.

## III. RESULTS

In this section we present results on the counting performance of HPCD pixels when subject to ultrafast exposures over a range of electron dose conditions when operating in normal and retrigger mode. This provides the data necessary to build a model for experimental uncertainties over a wide range of operating conditions. Starting from a Bernoulli counting experiment in a single pixel, the model is extended to give an expression for the uncertainty in the differential signals (differential mean count rate) obtained in ultrafast electron diffraction patterns under the entire relevant range of illumination conditions. At every step the model is compared to experimental results.

### A. Pixel response to ultrafast exposure

We obtained single-shot ultrafast exposures of the defocused electron beam under photocathode UV-excitation conditions that exposed the detector to electron dose conditions of  $10^{-3}$  to 10 at 1 kHz pulse repetition rate. Typical single-pixel count distributions obtained under low (0.16 EPP), medium (1.04 EPP) and high (7.6 EPP) average count rates acquired in normal and retrigger mode are shown in Fig. 2. At 0.16 EPP typical pixel-count distributions are in quantitative agreement with the Poisson distribution for  $k = 0$  and  $k = 1$  in both modes (shown in Fig. 2 a,d), but in disagreement for  $k = 2$  count events. Of the 2,000 single-shot frames processed, zero two-count events are registered in normal mode and only two registered in retrigger mode. Fifteen two-count frames are expected. Since normal-mode operation registers only a single count regardless of the number of electrons striking a pixel in a shot, zero two-counts are expected. Further, the  $k = 1$  counts in the normal mode histograms must be interpreted as corresponding to any  $k \geq 1$  event, so we compare the  $k = 1$  events against the predictions of the Poisson distribution integrated over  $k \geq 1$  in Fig. 2 a–c. At 1.04 EPP the typical-pixel count distribution in retrigger mode is in quantitative disagreement with the Poisson distribution at all count levels although some  $k = 2$  events are clearly registered. The histogram obtained

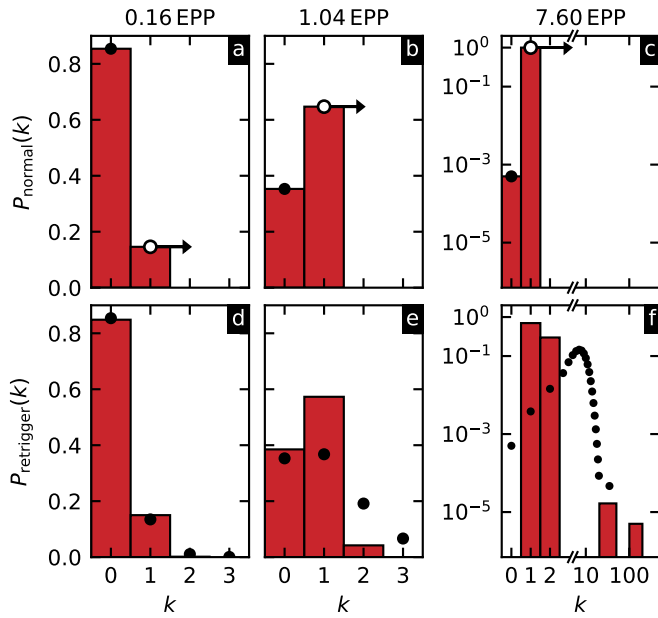


FIG. 2. Histograms of single-pixel count distributions  $P_{\text{normal}}(k)$  in normal (a–c) and  $P_{\text{retrigger}}(k)$  in retrigger (d–f) counting modes under low (a,d), intermediate (b,e), and high (c,f) electron doses. The incident electron count rates extracted with  $P_0$  counting are 0.16, 1.04 and 7.6 EPP, respectively.  $P_{\text{normal}}(k)$  denotes the normalized probability distribution such that  $\sum_k P_{\text{normal}}(k) = 1$ . The black points show the expected Poisson distribution for a mean value  $\lambda$  extracted with the  $P_0$  method from the normal-mode data; black circles in (a–c) truncate counts  $\geq 1$  as equivalent to 1. Note that in panels (c) and (f), the horizontal axis is linear for  $k \leq 3$  and logarithmic for larger values.

in normal mode is still in quantitative agreement with Poisson when the  $k = 1$  bin is understood as described above.

At 7.6 EPP the typical-pixel count distribution obtained in retrigger mode shows dramatic departures from a Poisson distribution. No frames containing 3–10 counts (or zero counts) are obtained, with some events (apparently random) registered with unphysical values exceeding 100. The histogram obtained in normal mode is, however, still in quantitative agreement with Poisson even under electron dose conditions where most frames register a count.

The sum of the retriggered histogram is approximately 3% lower than that of the expected Poisson distribution in the low count case, and approximately 37% lower in the medium count case. In the high count regime, such comparison is not meaningful due to the retrigger mode induced erroneous counts. We conclude that the retrigger mode of the detector is not suitable for UED(S) applications. Count losses are not significantly reduced in retrigger mode when ultrafast exposures are used. Further, retrigger mode also introduces random counting artifacts that add significant noise to the signals measured at all electron-dose levels when using ultrafast exposures. These artifacts can only be (partially) corrected by processing all single-shot images. Thus, all remaining data presented in this article were acquired in normal counting mode of the Dectris Quadro. A further analysis of the implica-

tions of using the retrigger mode is presented in Appendix A.

## B. Electron Counting

In the previous section we showed that only normal-mode readout of HPCDs provides artifact-free counting in ultrafast applications. Even in normal mode, only zero count events can be relied on quantitatively; i.e. pixels that register a count should be understood as having measured 1 count or more. Given these constraints, we discuss strategies to optimize measurement uncertainties when using a direct electron detector in ultrafast applications. First, for a single pixel and then for scattering signals across detectors.

### 1. Single Pixel Counting

In a single-shot, normal-mode image, all pixels have a value of either 0 or 1 even at high electron dose where Poisson statistics predict a high likelihood of multiple electrons arriving at the pixel in a single shot, as shown in Fig. 2 a–c. In this section we address the question of the most reliable method for estimating pixel signal levels under such constraints and the limits to dynamic range with current HPCDs in ultrafast applications.

Since each pixel has its own readout ASIC, we can treat individual pixels as independent detectors and derive some fundamental properties. The Poisson distribution determines the probability of detecting  $k$  electrons in a pixel per shot when the mean value is  $\lambda$  (i.e.  $[\lambda] = \text{EPP}$ ):

$$P_k(\lambda) = \frac{\lambda^k e^{-\lambda}}{k!}. \quad (1)$$

With a binary detector that reports a value of 0 for  $k = 0$  and a value of 1 for all  $k > 0$ , simple integration of detector counts leads to increasingly large losses of true electron counts for doses  $> 0.1$  EPP when multiple electron-count shots become increasingly common. However, zero-count events are reliably measured by the detector well into this range as shown in Fig. 2 a–c. Thus, the fraction of zero-count events to total events provides a more reliable way to estimate the mean of the Poisson distribution for larger electron doses:

$$\lambda = -\ln(P_0) = -\ln\left(\frac{\#\text{zeros}}{\#\text{total}}\right). \quad (2)$$

In what follows, this will be referred to as  $P_0$  counting for the determination of  $\lambda$ . To estimate the uncertainty of the  $P_0$  counting method we define a Bernoulli variable

$$X_i = \begin{cases} 1, & \text{if no electron detected} \\ 0, & \text{otherwise} \end{cases} \quad (3)$$

and measure the fraction of zero-events as the sum of independent Bernoulli variables

$$\hat{P}_0 = \frac{\#\text{zeros}}{\#\text{total}} = \frac{1}{N} \sum_{i=1}^N X_i. \quad (4)$$

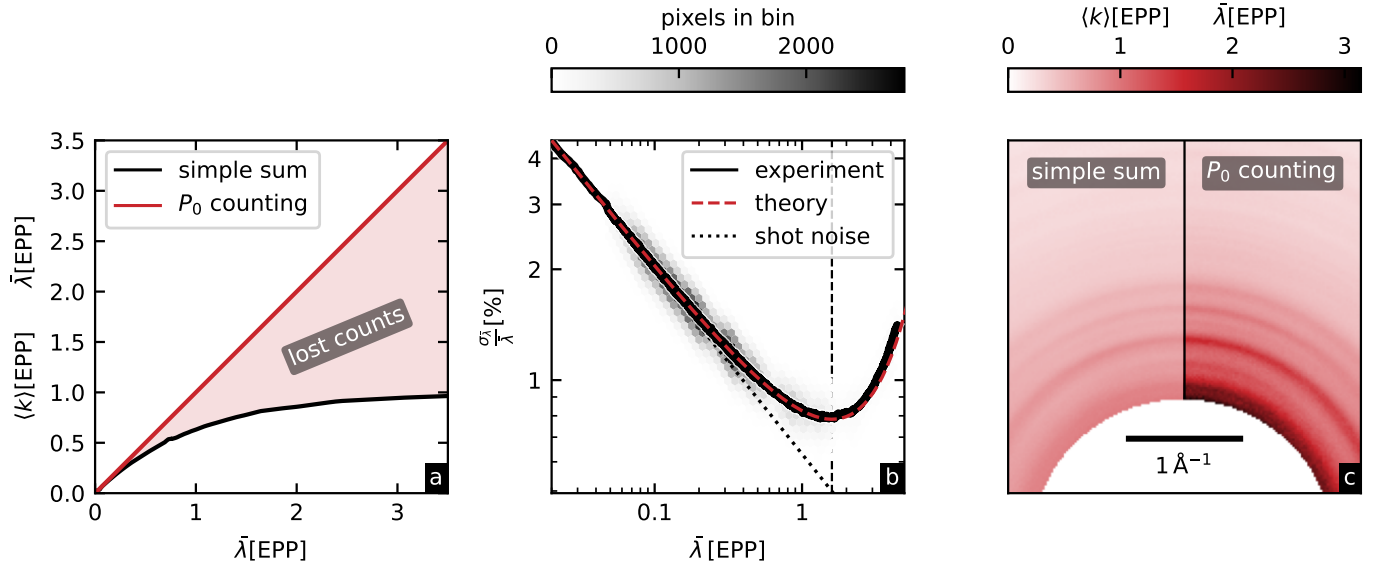


FIG. 3. **a** Detected per-pixel electron count rate in EPP using simple summation (black) and from  $P_0$  counting (red) against the rate estimated by  $P_0$  counting  $\bar{\lambda}$ . **b** Relative uncertainty in the per-pixel electron count rate versus  $\bar{\lambda}$  for  $P_0$  counting. The background heatmap shows the experimentally measured uncertainties from the data-set described in the text, with the corresponding colour bar at the top. A moving average of the experimental data is shown as a black solid line. The theoretical prediction from Eq. 6 is shown in red. The theoretical optimum (minimum uncertainty) electron count rate is marked with a vertical dashed line. The contribution from the fundamental shot-noise limit decreases with increasing beam current and is plotted as a dotted black line. **c** Diffraction pattern of polycrystalline monoclinic  $\text{VO}_2$ . The left image half was processed by simple summation and subject to lost counts. The right half was processed by analyzing the ratio of zero events  $\hat{P}_0$  and extracting  $\bar{\lambda}$ .

The variance of  $\hat{P}_0$  is

$$\text{Var}(\hat{P}_0) = \text{Var}\left(\frac{1}{N} \sum_i^N X_i\right) = \frac{1}{N^2} \sum_i^N \text{Var}(X_i) = \frac{P_0(1-P_0)}{N}. \quad (5)$$

Propagating to the estimator  $\hat{\lambda} = -\ln(\hat{P}_0)$  yields the relative uncertainty

$$\frac{\sigma_{\hat{\lambda}}}{\hat{\lambda}} = \frac{1}{\hat{\lambda}} \left| \frac{d}{dP_0} (-\ln(P_0)) \right| \sqrt{\text{Var}(P_0)} = \frac{1}{\hat{\lambda}} \sqrt{\frac{1-e^{-\lambda}}{e^{-\lambda}N}} \quad (6)$$

A minimum in relative uncertainty is reached for an expectation value of  $\lambda_{\text{opt}} = 1.5936$ , regardless of the total number of events  $N$ . Evaluating the relative uncertainty yields  $\frac{\sigma_{\hat{\lambda}}}{\hat{\lambda}}(\lambda_{\text{opt}} = 1.5936, N) = \frac{1.2426}{\sqrt{N}}$ . This gives an effective upper bound on the dynamic range of current HPCDs in ultrafast applications, since the relative uncertainty increases toward both the high- and low-dose extremes. Above an electron dose of 2 EPP the relative uncertainty in the mean count rate determination rapidly increases with the  $P_0$  counting method, diverging from the shot-noise limit, but remaining below 3% up to 7 EPP. In the lower limit, Eq. 6 asymptotes to the expected value for shot noise  $\frac{\sigma_{\hat{\lambda}}}{\hat{\lambda}} = \frac{1}{\sqrt{\lambda N}}$ .

A side-by-side comparison of simple integration of counts and  $P_0$  counting in a diffraction pattern of  $\text{VO}_2$  is shown in Fig. 3c. The contrast in the diffraction rings is strongly enhanced by  $P_0$  counting due to the strong loss of counts in bright pixels. The dataset is a series of 25,200 diffraction patterns taken at a 1 kHz repetition rate. For each pixel, we plot

the mean estimated  $\bar{\lambda}$  obtained by averaging per-stack estimates  $\hat{\lambda}$  over stacks of  $N = 400$  images. To further illustrate the suppression of the bright features, Fig. 3a shows the detected rate from both methods versus the mean of the rates estimated by  $P_0$  counting,  $\bar{\lambda}$ . At low electron flux both methods agree; at higher count rates they diverge because simple summation scales as  $1 - e^{-\lambda}$ . To verify this we compute the relative standard deviation across  $K$  independent stacks of  $N$  images

$$\frac{\sigma_{\bar{\lambda}}}{\bar{\lambda}} = \frac{1}{\bar{\lambda}} \sqrt{\frac{\sum_i^K (\hat{\lambda}_i - \bar{\lambda})^2}{K}} \quad (7)$$

where  $\hat{\lambda}_i$  is the per-stack estimate and  $\bar{\lambda}$  is their mean. The excellent agreement between prediction and experiment is depicted in Fig. 3b. A range of electron count rates from 0 to 3 EPP is covered, and the theoretical minimum appears at the predicted location.

## 2. Counting Across the Detector

Because of the potential large dynamic range in scattering patterns, it is not always possible to tune the beam current for minimum uncertainty across the recorded pattern. When looking at Figure 3a it becomes obvious that it is much more favourable to choose an electron beam current such that the brightest features of interest fall near the optimal per-pixel

count rate, because overexposed pixels have a stronger negative impact on the data than underexposed ones.

Samples that produce Debye-Scherrer rings, like polycrystalline materials or textured films, generate more homogeneously distributed scattering intensities that only depend on the magnitude of the scattering vector  $q = |\mathbf{q}|$ . This means that the intensity  $I(q)$  is equivalently measured by multiple pixels located at different azimuthal angles with same  $q$ . By averaging over  $M(q)$  such physically equivalent pixels, the measurement uncertainty in the mean intensity improves by a factor of  $\sqrt{M(q)}$ . Under our experimental geometry, diffraction from a VO<sub>2</sub> sample results in  $\{574, 761, 872, 1106\}$  pixel-centres lying within a  $\pm 0.025 \text{ \AA}^{-1}$  range of the  $\{(0\bar{1}1), (200), (0\bar{2}1), (220)\}$  diffraction ring centres. Azimuthally integrating the diffraction pattern improves the measurement uncertainty dramatically.

### C. Additional Noise Contributions

A complete description of the SNR of electron scattering experiments requires a consideration of noise sources beyond the counting-related detection noise described in the previous section. Kealhofer et al.<sup>25</sup> investigated the signal-to-noise ratio of ultrafast electron diffraction experiments using a CCD detector and described the total noise in terms of a number of independent factors:

$$\sigma_{\text{total}} = \sqrt{\sigma_{\text{counting}}^2 + \sigma_{\text{source}}^2 + \sigma_{\text{gain}}^2 + \sigma_{\text{int}}^2 + \sigma_{\text{read}}^2} \quad (8)$$

Some of the noise contributions that must be considered for a CCD detector are negligible for HPCDs, namely gain, integration and readout noise  $\{\sigma_{\text{gain}}, \sigma_{\text{int}}, \sigma_{\text{read}}\}$ . The per-pixel ASIC architecture of the HPCD reads images with virtually no readout and gain noise. Noise due to integration is also not accumulated, since one image is recorded per electron bunch and the integration happens digitally. Thus, only source and counting-related noise remain. In Appendix A we provide a quantitative justification for this approximation of Eq. 8. Counting related noise is bound by shot-noise at low electron doses and by  $P_0$  counting uncertainties at  $\bar{\lambda} > 1 \text{ EPP}$  as demonstrated in the previous section (Fig. 3 b). Here we investigate the relative contribution of source noise and counting noise to the total integrated electron scattering signal obtained from a 10 nm-thick polycrystalline Pt film on a free-standing 50 nm SiN membrane (undiffracted beam excluded). Simultaneously, we recorded the pulse energy of the laser amplifier output with a photodiode and a boxcar integrator.

Over 500 s a total of  $N_{\text{samp}} = 500,000$  single-shot diffraction patterns and photodiode signals were collected. The count rate within the analyzed region of the electron diffraction pattern (outside the undiffracted beam) ranges from 0.15 to 0.03 EPP, well within the low electron-dose limit where a negligible number of counts are lost by the detector and counting is fundamentally limited by shot noise. The average total diffraction pattern counts per shot (i.e. counts outside the transmitted beam)  $\langle \mathcal{I} \rangle$  was 14,700. The expected shot-noise on the average total diffraction pattern counts is 0.82%, while

the measured standard deviation of the total diffraction pattern counts was slightly higher at 1.05% due to the presence of source noise.

Power spectral densities of both signals  $S(t)$  are obtained by taking the real Fourier-transform of the relative intensity noise (RIN)

$$S(f) = \frac{2}{N_{\text{samp}} \Gamma} \left| \mathcal{FT} \left\{ \frac{S(t) - \langle S \rangle}{\langle S \rangle} \right\} (f) \right|^2 \quad (9)$$

and shown in Fig. 4 a.

The overall RIN fluctuations in the fundamental laser signal are around 0.14% and noticeably lower than the fluctuations in the total electron counts. This noise amplification arises from the nonlinear behaviour of the third-harmonic generation setup that converts the IR pulses from the amplifier into UV pulses that generate the electron bunches.

The high-frequency noise floor of the single-shot diffraction pattern-counts approaches the fundamental shot-noise limit inherent to discrete electron detection,  $\frac{2}{\Gamma \langle \mathcal{I} \rangle}$ . The low-frequency behaviour of the process can be modelled using a pink noise model  $S(f) = \frac{A}{f^\alpha} + C$ , with an amplitude  $A$  and an exponential scaling factor  $\alpha$  and a constant offset  $C$ . Using the fundamental shot-noise limit as the offset we recover an exponential scaling factor of  $\alpha = 1.02$ , which resembles an almost fundamental PSD observed in a wide range of semiconductor devices and amplifiers. The fitted PSD is plotted as a blue dashed line in Fig. 4 a. Integrated over the range of frequencies shown, shot noise accounts for  $\approx 60\%$  of the variation and source noise 40% at  $\langle \mathcal{I} \rangle = 14,700$

To determine how the source noise contribution can be expected to scale with  $\langle \mathcal{I} \rangle$  and integration time-window, we add a multiplicative source-noise jitter to our model to describe the bunch-charge fluctuations. We represent these as a frame-wise scaling factor  $Y$  that multiplies entire diffraction pattern in a given exposure. To leave the unconditional mean diffraction image unchanged, we take  $\mathbb{E}[Y] = 1$  and define the RIN of the electron source on the relevant timescales as  $\epsilon^2 = \text{Var}(Y)$ . Conditioned on  $Y$ , we assume independent pixel counting with

$$I_{ij} | Y \sim \text{Poisson}(Y \bar{I}_{ij}). \quad (10)$$

Here  $\bar{I}_{ij}$  is the mean intensity pattern in pixel  $(i, j)$  in the absence of source fluctuations. Under these assumptions we get the expectation value  $\mathbb{E}[I_{ij} | Y] = Y \bar{I}_{ij}$ , the variance  $\text{Var}(I_{ij} | Y) = Y \bar{I}_{ij}$ , and the covariance  $\text{Cov}(I_{ij}, I_{uv} | Y) = 0$  for  $(i, j) \neq (u, v)$ . Let the total electron count in an image be  $\mathcal{I} = \sum_{i,j} I_{ij}$ . Using the law of total variance and covariance, we write

$$\text{Var}(\mathcal{I}) = \sum_{i,j} \text{Var}(I_{ij}) + \sum_{(i,j) \neq (u,v)} \text{Cov}(I_{ij}, I_{uv}) \quad (11)$$

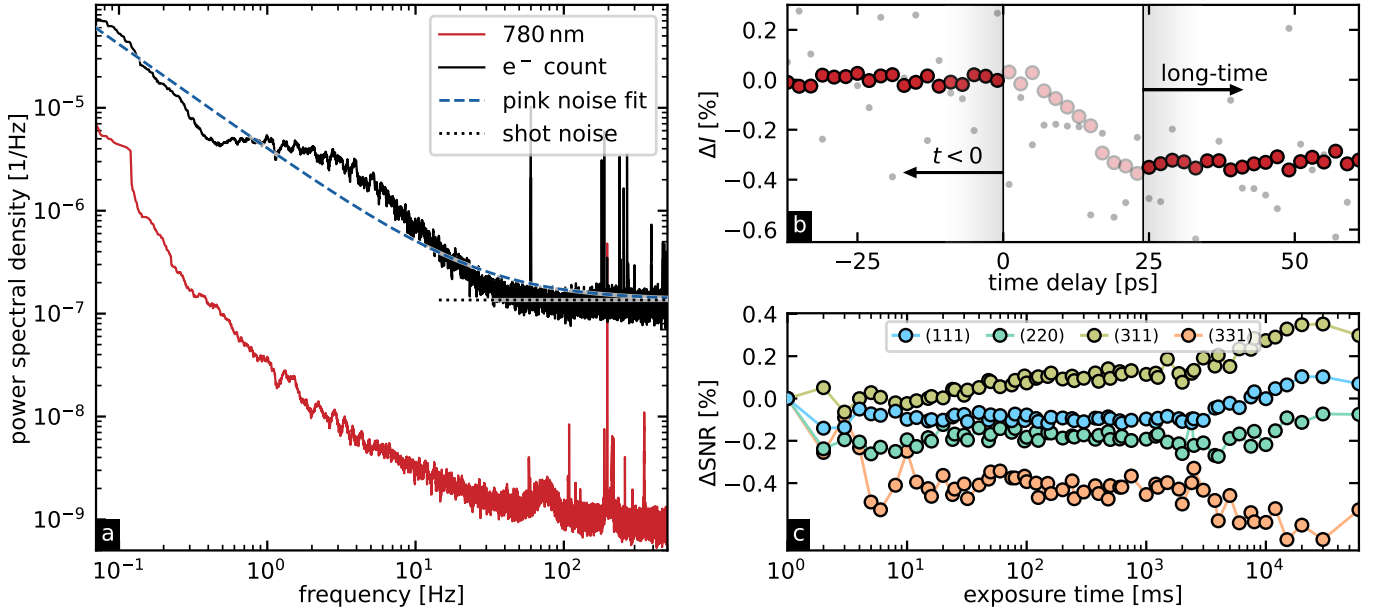


FIG. 4. **a** PSD of the fundamental 780 nm output from the laser amplifier (red) and the total scattered electron count (black). The black dashed line marks the shot-noise floor of the electron-count signal. The blue dashed line shows the fit to an  $1/f^\alpha$  noise model. **b** Transient diffraction signal for the (220) Debye-Scherrer ring from  $-30$  to  $60$  ps. For the SNR analysis we use the time ranges outside the two black vertical lines. The data has been normalized with a shot-to-shot scheme. The grey points in the background show the same transient signal without using any normalization. **c** Change in SNR versus simulated exposure time for four different Debye-Scherrer rings.

and expand each term via conditioning on  $Y$ :

$$\begin{aligned} \text{Var}(\mathcal{I}) &= \sum_{i,j} (\mathbb{E}_Y[\text{Var}(I_{ij}|Y)] + \text{Var}(\mathbb{E}_Y[I_{ij}|Y])) \\ &+ \sum_{(i,j) \neq (u,v)} \left( \mathbb{E}_Y[\text{Cov}(I_{ij}, I_{uv}|Y)] \right. \\ &\left. + \text{Cov}(\mathbb{E}_Y[I_{ij}|Y], \mathbb{E}_Y[I_{uv}|Y]) \right). \end{aligned} \quad (12)$$

The cross-pixel covariance  $\mathbb{E}_Y[\text{Cov}(I_{ij}, I_{uv}|Y)]$  vanishes after being conditioned on the common jitter  $Y$  and we simplify to

$$\begin{aligned} \text{Var}(\mathcal{I}) &= \sum_{i,j} (\bar{I}_{ij} + \text{Var}(Y\bar{I}_{ij})) \\ &+ \sum_{(i,j) \neq (u,v)} (0 + \text{Cov}(Y\bar{I}_{ij}, Y\bar{I}_{uv})). \end{aligned} \quad (13)$$

From here we can group a shot noise term, a source noise term, and a term from the cross-pixel covariance from source noise

$$\text{Var}(\mathcal{I}) = \sum_{i,j} \bar{I}_{ij} + \text{Var}(Y) \left( \sum_{i,j} \bar{I}_{ij}^2 + \sum_{(i,j) \neq (u,v)} \bar{I}_{ij} \bar{I}_{uv} \right) \quad (14)$$

$$= \sum_{i,j} \bar{I}_{ij} + \sum_{(i,j),(u,v)} \bar{I}_{ij} \bar{I}_{uv} \varepsilon^2 \quad (15)$$

$$\text{Var}(\mathcal{I}) = \bar{\mathcal{I}} + \text{Var}(Y) \bar{\mathcal{I}}^2. \quad (16)$$

Note that we did not make any assumption of the frequency signature of the noise and only assumed (i) multiplicative jitter and (ii) conditional Poisson counting. Eq. 16 separates shot

noise that is linear in  $\bar{\mathcal{I}}$  from excess source noise which is quadratic in  $\bar{\mathcal{I}}$ .

Assuming the source noise has a flat PSD (white noise) we can write  $Y \sim \mathcal{N}(1, \varepsilon^2)$  and simply write

$$\text{Var}(\mathcal{I}) = \bar{\mathcal{I}} + \bar{\mathcal{I}}^2 \varepsilon^2, \quad (17)$$

assuming small fluctuations  $\varepsilon \ll 1$ .

The model used to fit the PSD of the total electron counts in Fig. 4 a can be analyzed using a stationary fluctuating process with  $Y(t) = 1 + \delta(t)$  with a PSD

$$S_\delta(f) = \frac{A}{f^\alpha}, \quad f \in [f_L, f_H], \quad (18)$$

with the low-frequency cutoff  $f_L = \frac{1}{T}$  being the inverse of the measurement duration and the high-frequency cutoff  $f_H = \Gamma/2$  being half the laser repetition rate and an amplitude  $A$ . The variance of this process can be calculated by integrating the PSD as

$$\text{Var}(Y) = \text{Var}(\delta) = \int_{\frac{1}{T}}^{\frac{\Gamma}{2}} \frac{A}{f^\alpha} df. \quad (19)$$

Epsilon becomes  $T$ -dependent and slowly increases with measurement duration

$$\varepsilon^2(T) \equiv \text{Var}(\delta) = \frac{A}{1-\alpha} \left[ \left( \frac{\Gamma}{2} \right)^{1-\alpha} - \left( \frac{1}{T} \right)^{1-\alpha} \right]. \quad (20)$$

For true pink noise ( $\alpha = 1$ ) this simplifies to

$$\varepsilon^2(T) = A \ln(f_H T), \quad (21)$$

with the same slow logarithmic growth in  $T$ . In practice, our observables are formed by averaging repeated measurements acquired in randomized order, which suppresses slow drifts and makes the residual contribution of source noise well-captured by an effective white-noise RIN parameter  $\varepsilon$  as presented in Eq. 17. Consistent with this simplification we did not see a dependence of SNR on our normalization window from 1 ms to 1 min.

#### D. Image Normalization Strategies

Normalization of acquired UED(s) images is an important means to improve experimental SNR by reducing the impact of the source noise described in the previous section. The ability to perform full-frame readout above 1 kHz with HPCDs allows the exploration of shot-to-shot UED(S) data normalization strategies that have the potential to further improve SNR in UED(S) data, but have been impossible to implement with low frame-rate cameras due to the relatively long integration time required before image readout. Here we comprehensively investigate the impact of the (normalization) exposure time window on the SNR of pump-probe UED(S) data to see if significant benefits are obtained by moving towards a shot-to-shot normalization scheme in these experiments. To this end, we recorded a UED dataset from a 10 nm-thick polycrystalline Pt film on a freestanding 50 nm SiN membrane (the same sample investigated in the previous section), photoexcited with 150 fs laser pulses centered at 780 nm using a fluence of  $0.1 \frac{\text{mJ}}{\text{cm}^2}$  at 1 kHz repetition rate. We recorded a total of 60,000 single-shot diffraction images at 50 time-delay points, allowing the direct comparison of exposure times from single-shot to one minute using this single dataset. Handling single-shot datasets of this size requires efficient storage and integration techniques; a suggested implementation approach used by the authors is outlined in Appendix E.

From the transient differential diffraction intensity in a Debye-Scherrer ring

$$\Delta I(t) = \frac{I(t) - \langle I(t < 0) \rangle}{\langle I(t < 0) \rangle}, \quad (22)$$

we extract signal and noise to calculate the SNR per ring. An example transient signal is shown in Figure 4b for the (220) diffraction ring. Photoexcitation results in a rapid decrease in diffraction intensity due to the Debye-Waller effect, after which the diffracted intensity is approximately constant on the ps-timescale. We quantify long-time signal as  $\langle I(t > 25 \text{ ps}) \rangle$  and the pre-photoexcitation intensity  $\langle I(t < 0) \rangle$  as a baseline. The noise level is estimated from the standard deviation of the pre-photoexcitation time delays, yielding

$$\text{SNR} = \frac{|\langle I(t > 25 \text{ ps}) \rangle - \langle I(t < 0) \rangle|}{\sqrt{\frac{1}{N_T} \sum_{t < 0} (I(t) - \langle I(t < 0) \rangle)^2}}, \quad (23)$$

where  $N_T$  is the number of pre-photoexcitation samples.

To simulate the (normalization) exposure time window dependence on SNR, a variable number of single electron shot

diffraction patterns are first stacked before image normalization is performed and the transient differential intensity is computed. Given the experimental conditions, we are limited to 60 different exposure time windows between 1 ms and 1 min, because the stack of 60,000 images must be divided into equal parts. Overall results of this analysis are shown in Figure 4c. We find that SNR is constant within 0.5% over the whole simulated (normalization) exposure-time range. There is significant flexibility in the normalization time-window used in the treatment of UED(S) data. Shot-to-shot image acquisition and normalization followed by integration, or integrated (multi-shot) image acquisition followed by normalization are equally effective over a wide range of integration windows. Shot-to-shot image normalization does not provide a significant SNR advantage in UED(S) experiments. By contrast, simply eliminating image normalization altogether reduces the SNR by up to a factor of 4 depending on the brightness of the diffraction ring considered. Transient diffraction signals computed from unnormalized data are plotted on top of the normalized results in Fig. 4, and the serious deterioration in SNR is clearly evident. This work bridges the noise analysis performed in Kealhofer et al.<sup>25</sup> and Claude et al.<sup>26</sup>, where the benefits of image normalization were clearly demonstrated, but only shot-to-shot<sup>26</sup> or long-exposure time windows<sup>25</sup> were investigated.

This result is also in keeping with fundamental considerations under the assumption of (i) common multiplicative bunch-charge fluctuations, (ii) negligible additional cross-pixel correlations, and (iii) zero-mean jitter in a stationary process. Appendix B provides a derivation showing that the operation of normalization commutes with integration.

While the normalization time-window does not significantly impact the SNR acquired at low EPP, short integration windows can be problematic when extracting absolute electron count rates with the  $P_0$  method. Because  $P_0$  counting relies on  $\hat{\lambda} = -\ln(\hat{P}_0)$ , estimates formed from too few frames are biased upward by the convexity of the logarithm; Appendix C quantifies this bias. The practical implication is that the absolute dose estimates should be formed from observations using over a minimum of a few hundred, even though the normalization remains effective over the full exposure-time range.

In pump-probe measurements, however, we are mainly interested in changes in the scattering intensity. When the two estimates use a matched number of events and have similar count rates, most of the logarithmic bias cancels in the difference signal. Since those conditions are met in all of our measurements we will disregard the bias in the following. Should these conditions not be met, the bias is still predictable and can be corrected analytically using the derivation presented in Appendix C.

#### E. Total Experimental Uncertainty

Here we conduct UED(S) experiments in the electron dose regime where  $P_0$  counting becomes relevant to validate our model of the relative uncertainty in a single pixel from Sec-

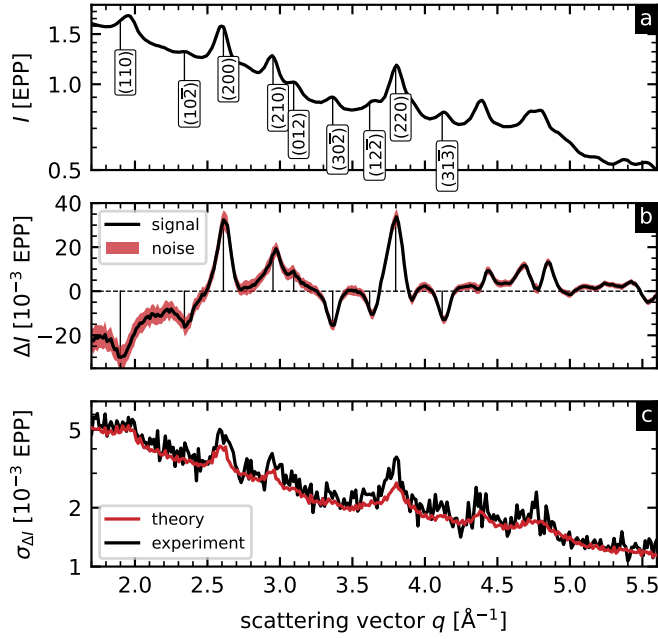


FIG. 5. **a** Absolute azimuthally averaged diffraction pattern of VO<sub>2</sub> in equilibrium. Selected diffraction rings are labelled with their respective Miller indices. **b** Photoinduced signal change in diffracted intensity between 11 and 86 ps after photoexcitation (black) and rms noise (red). **c** Absolute uncertainty in the detected signal change as measured (black) and predicted (red).

tion III B 1 together with the inclusion of additional source noise from Section III C. The UED dataset is investigating the transient diffraction  $I(q, t)$  of VO<sub>2</sub> under 780 nm photoexcitation with a fluence of  $16.6 \frac{\text{mJ}}{\text{cm}^2}$  and a reduced repetition of 200 Hz to counteract static heating. For each time-delay we recorded a stack of 500 single-shot diffraction images to estimate an electron dose for each pixel. This acquisition was repeated seven times and all images are azimuthally integrated into 1000  $q$ -bins to improve statistics. Across all time delays, we average negative time-delay data  $I(t < 0)$  and long time-delay data  $I(t > 11 \text{ ps})$ , analogous to Figure 4 b. The diffracted intensity before photoexcitation is shown in Fig. 5 a and the difference signal  $\Delta I(q) = \langle I(t > 11 \text{ ps}) \rangle - \langle I(t < 0) \rangle$  in Fig. 5 b.

For the experimental uncertainty per  $q$ -bin, we compute the standard error of the difference of two independently averaged quantities. Let  $K_-$  and  $K_+$  denote the number of stacks contributing to the pre- and long-excitation averages, respectively. Furthermore, let  $\sigma_{\pm}(q)$  be the standard deviations across stacks of the per-stack estimates in the  $q$ -bin. The standard error of the difference is

$$\sigma_{\Delta, \text{exp}}(q) = \sqrt{\frac{\sigma_-^2(q)}{K_-} + \frac{\sigma_+^2(q)}{K_+}}. \quad (24)$$

This experimentally measured uncertainty is shown as a red error band around the differential diffraction signal in Fig. 5 b. To model the same quantity theoretically, we treat frame-to-frame bunch-charge fluctuations as Gaussian jitter of the instantaneous Poisson rate as discussed in Section III C. The

key step is to combine the single-pixel uncertainty model with the source-noise assumptions made earlier. In Appendix D we propagate the common multiplicative jitter from source noise through the  $P_0$  estimator that is formed from  $N$  events and averaged azimuthally over  $M$  pixels. As a result of the derivation we find that the uncertainty separates into a counting term that improves with the number of trials  $NM$  and a source-noise term that remains correlated across pixels and hence only improves with  $N$ . Applying the delta method yields the expected uncertainty for a  $P_0$  counting based measurement in a given  $q$ -bin, over  $K_{\pm}$  independent stacks gives (see Eqs. D15, D16):

$$\sigma_{\mp, \text{th}} = \frac{e^{\bar{\lambda}}}{\sqrt{K_{\mp}}} \sqrt{\frac{e^{-\bar{\lambda} + \frac{1}{2}\epsilon^2} - e^{-2\bar{\lambda} + \epsilon^2}}{MN} + \frac{e^{-2\bar{\lambda} + 2\epsilon^2} - e^{-2\bar{\lambda} + \epsilon^2}}{N}}, \quad (25)$$

using the source-noise estimate  $\epsilon = 0.65\%$  from Section III C and using  $M(q) \gg 1 \forall q$ . In a last step, inserting Eq. 25 into Eq. 24 yields the full expression for the model uncertainty of a difference signal. Panel c overlays  $\sigma_{\Delta, \text{exp}}(q)$  (black) with  $\sigma_{\Delta, \text{th}}(q)$  (red). The agreement across the entire  $q$ -range is good, confirming that the  $P_0$  counting model accurately captures the statistical uncertainty and the data is shot-noise limited after normalization and aggregation over all frames of a stack, equivalent pixels, and time-delays. Practically, this provides a simple planning tool for ultrafast electron diffraction experiments.

#### IV. CONCLUSIONS

HPCDs can be a powerful tool for collecting UED(S) data without readout and dark noise, but HPCD pixels suffer saturation in ultrafast applications at the level of  $\approx 1$  detected electron per pulse. The available retrigger modes on these detectors do not alleviate this problem and only introduce additional noise sources. This places an important upper limit on the detector dynamic range, as counts/second in the brightest features cannot exceed the pulse repetition rate without introducing counting uncertainties in excess of shot-noise limits. Ultrafast exposures subject HPCDs to profoundly different conditions than continuous beam experiments; i.e. the waiting time between subsequent counts in a pixel is exponentially distributed for continuous beams, but is effectively zero within a single ultrafast exposure.

Thus, these detectors excel when detecting very weak signals (phonon-diffuse) and collecting patterns with a moderate dynamic range, such as gas-phase samples, polycrystalline materials, or textured films, where the scattered intensity is well distributed over the detector, and even the brightest current ultrafast electron sources can just reach a count rate of 1 EPP. Under such circumstances, detection of UED signals at the shot-noise limit is easily obtained with HPCDs. In single crystal experiments, however, Bragg peak features can easily saturate the detector and count losses adversely impact sensitivity. Ideally, HPCDs with charge integrating ASICs rather than threshold circuitry could be developed to reliably count

multiple electrons inside a single shot, overcoming the limitations of this technology at the high end of the dynamic range for ultrafast applications. Detector gating, which is straightforward in ultrafast applications through synchronization with the laser pulse train, could simplify such developments.

At source noise levels typical of current generation UED instruments, SNR in UED is not significantly improved by shot-to-shot normalization enabled by the high frame rates. SNR is virtually independent of the normalization time window. Normalization shot-by-shot or after stack integration does not affect the SNR.

## V. ACKNOWLEDGEMENTS

L. K. gratefully acknowledges support from a Fonds de Recherche du Quebec-Nature et Technologies (FRQNT) Merit fellowship. B. J. S. gratefully acknowledges the support of the Canada Research Chairs program. This work was supported by the FRQNT, the Canada Foundation for Innovation (CFI), and the National Research Council of Canada (NRC) Collaborative R&D program (Quantum Sensors)

## VI. AUTHOR DECLARATIONS

The authors have no conflicts of interest to disclose.

## VII. DATA AVAILABILITY

The data that support the findings of this study are available from the corresponding author upon reasonable request.

- <sup>1</sup>D. Filippetto, P. Musumeci, R. K. Li, B. J. Siwick, M. R. Otto, M. Centurion, and J. P. F. Nunes, *Rev. Mod. Phys.* **94**, 045004 (2022).
- <sup>2</sup>G. Sciaini and R. J. D. Miller, *Reports on Progress in Physics* **74**, 096101 (2011).
- <sup>3</sup>P. Maldonado, T. Chase, A. H. Reid, X. Shen, R. K. Li, K. Carva, T. Payer, M. Horn von Hoegen, K. Sokolowski-Tinten, X. J. Wang, P. M. Oppeneer, and H. A. Dürr, *Physical Review B* **101**, 10.1103/physrevb.101.100302 (2020).
- <sup>4</sup>S. R. Tauchert, M. Volkov, D. Ehberger, D. Kazenwadel, M. Evers, H. Lange, A. Donges, A. Book, W. Kreuzpaintner, U. Nowak, and P. Baum, *Nature* **602**, 73–77 (2022).
- <sup>5</sup>T. L. Britt, Q. Li, L. P. René de Cotret, N. Olsen, M. Otto, S. A. Hassan, M. Zacharias, F. Caruso, X. Zhu, and B. J. Siwick, *Nano Letters* **22**, 4718–4724 (2022).
- <sup>6</sup>M. Harb, H. Enquist, A. Jurgilaitis, F. T. Tuyakova, A. N. Obraztsov, and J. Larsson, *Phys. Rev. B* **93**, 104104 (2016).
- <sup>7</sup>L. Kremeyer, T. L. Britt, B. J. Siwick, and S. C. Huberman, *Structural Dynamics* **11**, 10.1063/4.0000224 (2024).
- <sup>8</sup>H. Ehrke, R. I. Tobey, S. Wall, S. A. Cavill, M. Först, V. Khanna, T. Garl, N. Stojanovic, D. Prabhakaran, A. T. Boothroyd, M. Gensch, A. Mirone, P. Reutler, A. Revcolevschi, S. S. Dhési, and A. Cavalleri, *Phys. Rev. Lett.* **106**, 217401 (2011).
- <sup>9</sup>Y. Cheng, A. Zong, L. Wu, Q. Meng, W. Xia, F. Qi, P. Zhu, X. Zou, T. Jiang, Y. Guo, J. van Wezel, A. Kogar, M. W. Zuerch, J. Zhang, Y. Zhu, and D. Xiang, *Nature Physics* **20**, 54–60 (2024).
- <sup>10</sup>C. Dornes, Y. Acremann, M. Savoini, M. Kubli, M. J. Neugebauer, E. Abreu, L. Huber, G. Lantz, C. A. F. Vaz, H. Lemke, E. M. Bothschafter, M. Porer, V. Esposito, L. Rettig, M. Buzzi, A. Alberca, Y. W. Windsor, P. Beaud, U. Staub, D. Zhu, S. Song, J. M. Glowina, and S. L. Johnson, *Nature* **565**, 209–212 (2019).
- <sup>11</sup>A. Kogar, A. Zong, P. E. Dolgirev, X. Shen, J. Straquadine, Y.-Q. Bie, X. Wang, T. Rohwer, I.-C. Tung, Y. Yang, R. Li, J. Yang, S. Weathersby, S. Park, M. E. Kozina, E. J. Sie, H. Wen, P. Jarillo-Herrero, I. R. Fisher, X. Wang, and N. Gedik, *Nature Physics* **16**, 159–163 (2019).
- <sup>12</sup>V. R. Morrison, R. P. Chatelain, K. L. Tiwari, A. Hendaoui, A. Bruhács, M. Chaker, and B. J. Siwick, *Science* **346**, 445–448 (2014).
- <sup>13</sup>D. N. Basov, R. D. Averitt, and D. Hsieh, *Nature Materials* **16**, 1077–1088 (2017).
- <sup>14</sup>T. LaGrange, P. Cattaneo, B. Barwick, D. J. Flannigan, J. Weissenrieder, and F. Carbone, *Nature Reviews Methods Primers* **5**, 61 (2025).
- <sup>15</sup>Dynamic range extracted from data of<sup>27</sup>.
- <sup>16</sup>T. Domröse, L. da Camara Silva, and C. Ropers, *Applied Physics Letters* **126**, 10.1063/5.0266507 (2025).
- <sup>17</sup>M. W. Tate, P. Purohit, D. Chamberlain, K. X. Nguyen, R. Hovden, C. S. Chang, P. Deb, E. Turgut, J. T. Heron, D. G. Schlom, *et al.*, *Microscopy and Microanalysis* **22**, 237 (2016).
- <sup>18</sup>F. Barantani, R. Claude, F. Iyikanat, I. Madan, A. A. Sapozhnik, M. Puppini, B. Weaver, T. LaGrange, F. J. G. de Abajo, and F. Carbone, *Science advances* **11**, ead1001 (2025).
- <sup>19</sup>Y.-J. Kim, L. D. Palmer, W. Lee, N. J. Heller, and S. K. Cushing, *The Journal of Chemical Physics* **159**, 10.1063/5.0147356 (2023).
- <sup>20</sup>*User Manual Dectris Quadro*, Dectris Ltd, Baden-Daettwil, Switzerland, v1.7.2 ed. (2021).
- <sup>21</sup>A. Förster, S. Brandstetter, and C. Schulze-Briese, *Philosophical Transactions of the Royal Society A: Mathematical, Physical and Engineering Sciences* **377**, 20180241 (2019).
- <sup>22</sup>T. Loeliger, C. Brönnimann, T. Donath, M. Schneebeli, R. Schnyder, and P. Trüb, in *2012 IEEE Nuclear Science Symposium and Medical Imaging Conference Record (NSS/MIC)* (2012) pp. 610–615.
- <sup>23</sup>R. P. Chatelain, V. R. Morrison, C. Godbout, and B. J. Siwick, *Applied Physics Letters* **101**, 081901 (2012).
- <sup>24</sup>M. R. Otto, L. René de Cotret, M. J. Stern, and B. J. Siwick, *Structural Dynamics* **4**, 10.1063/1.4989960 (2017).
- <sup>25</sup>C. Kealhofer, S. Lahme, T. Urban, and P. Baum, *Ultramicroscopy* **159**, 19 (2015).
- <sup>26</sup>R. Claude, M. Puppini, B. Weaver, P. Usai, T. LaGrange, and F. Carbone, *Structural Dynamics* **12**, 10.1063/4.0000775 (2025).
- <sup>27</sup>L. P. René de Cotret, J.-H. Pöhl, M. J. Stern, M. R. Otto, M. Sutton, and B. J. Siwick, *Phys. Rev. B* **100**, 214115 (2019).
- <sup>28</sup>C. Ma and L. Ying, *Research in the Mathematical Sciences* **12**, 10.1007/s40687-024-00483-6 (2025).
- <sup>29</sup>M. Banahan, D. Brady, and M. Doran, *The C Book, Featuring the ANSI C Standard* (Addison-Wesley Publishing Company, 1991) Chap. 6.4 Bitfields.
- <sup>30</sup>K. Masui, M. Amiri, L. Connor, M. Deng, M. Fandino, C. Höfer, M. Halpern, D. Hanna, A. D. Hincks, G. Hinshaw, J. M. Parra, L. B. Newburgh, J. R. Shaw, and K. Vanderlinde, *Astron. Comput.* **12**, 181 (2015).
- <sup>31</sup>P. Deutsch, *GZIP file format specification version 4.3*, Tech. Rep. (IETF, 1996).

## Appendix A: Electron Detector Counting Details

This part of the appendix discusses experimental details of electron counting, such as dark-count rates and unphysical pixel values.

*Dark Counts*—To quantify readout noise and dark counts in our setup we take images without exposing the detector to electrons. Over a total time span of 7 hours, 30 stacks of 15,000 images each were taken, resulting in 450,000 total images. The total counts in those images are 852, detected randomly across the detector over time. Spatially, one observes randomly distributed noise and a few streaks due to cosmic background radiation. No pixel recorded more than two total counts. On average, the probability of a pixel registering a

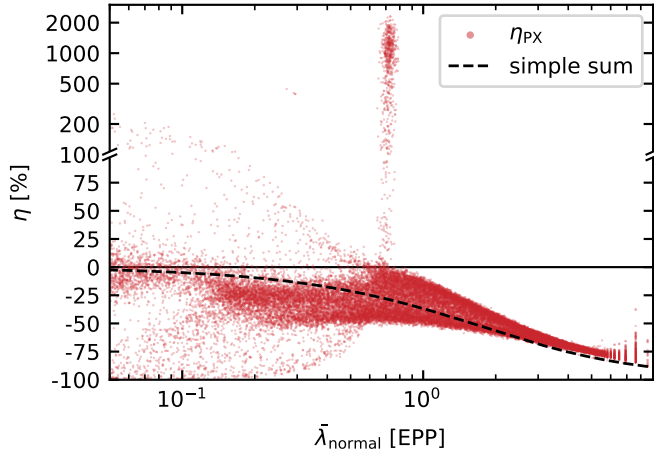


FIG. 6. Scatter plot for the gain/loss behaviour when using retrigger versus normal trigger mode. Each scattered point corresponds to a pixel and the vertical axis is linear between  $-100$  and  $100\%$ , for larger positive values the axis is logarithmically scaled.

dark count for a single exposure is

$$P_{\text{dark}} = \frac{\text{\#counts}}{\text{\#images} \cdot \text{\#pixels}} = 7.6 \times 10^{-9}, \quad (\text{A1})$$

which is negligible compared to other sources of noise in the experiment.

*Non-binary events*—Approximately 1% of the pixels in a dataset produce unphysical values of  $2^{16} - 1$  counts. These defective pixels are masked during data processing. Among the remaining pixels, only a very small fraction exhibit non-binary counts. Specifically, we observe a fraction of  $\frac{\text{\#}(N>1)}{\text{\#}N} \approx 5 \times 10^{-7}$ . During data processing, all such non-binary events that are not masked are set to a value of 1.

*Retrigger Mode*—The behaviour of the retrigger mode of the electron detector has been discussed on a single-pixel basis in Section III A. Especially noting the pathological values obtained from the detector in retrigger mode, we look the behaviour across the detector with respect to incident electron flux. In the discussion we will use the count rate estimated with the  $P_0$ -method in normal mode as a baseline and obtain a reading in retrigger mode via a simple sum of all events. The gain/loss can then be evaluated as  $\eta = \frac{\bar{\lambda}_{\text{retr}}}{\bar{\lambda}_{\text{normal}}} - 1$ . From the discussion in the main text, we expect both modes to behave similarly in the low electron flux regime; with increasing flux we expect an increase in lost counts, i.e. a decrease in  $\eta$ , since the electron bunches are much shorter than the pixel dead time.

To investigate this, the gain/loss  $\eta$  versus  $\bar{\lambda}_{\text{normal}}$  is plotted for every pixel in Fig. 6 using the same experimental conditions as in Section III A. While an accumulation of points around  $\eta = 0$  can be seen, and a pronounced tail towards higher electron fluxes describes the loss of counts, there are many outliers. Very pronounced is an almost vertical tail at  $0.7$  EPP that show pathological gains of up to  $2,000\%$ . We infer that those come from the pathological count that we presented in Fig. 2f of the main text. As a guide the loss for a simple summation of counts in a binary detector is shown

with a dashed line, since that is the expected model outcome for a retriggered pixel that fails in detecting multiple counts. Although in the regime of 1 to 6 EPP there are only few outliers, the loss is not as pronounced as it would be if the retriggered detector did not pick up any multi-electron doses. This small effect is noticeable but not useful for conducting experiments. The conclusion from investigating the *instant retrigger technology* is that it is not suitable for applications in ultrashort compressed electron bunch environments and leads to corrupted data.

## Appendix B: Normalization w.r.t. Exposure Time

Suppose conducting a measurement of true diffraction signal  $S_{ij}$  across the detector in pixel space  $\{i, j\}$  with a total intensity  $\sum_{i,j} S_{ij} = 1$ , probed with a mean electron bunch charge  $Q_B$  and a shot-to-shot jitter  $\delta_k$  in shot  $k$ . The relative intensity jitter  $R_\delta(m)$  can be related to the PSD of the source  $\Phi_\delta(f)$ :

$$R_\delta(m) = \text{Cov}(\delta_k, \delta_{k+m}), \quad (\text{B1})$$

$$\Phi_\delta(f) = \sum_{m=-\infty}^{\infty} R_\delta(m) e^{-i2\pi f m / \Gamma}, \quad (\text{B2})$$

with the integer shot distance  $m$ .  $\Phi_\delta(f)$  for our experiment is shown in Fig. 4 a. We assume no systematic drift in intensity  $\langle \delta_k \rangle = 0$ , and a stationary process ( $R_\delta(m) \neq f(k)$ ), i.e.  $R_\delta(m)$  only depends on the lag  $m$ . Normalizing images over the intensity of an image stack of size  $N$  results in a normalized image

$$I_{ij}^c = \frac{T_{ij}}{T_{\text{tot}}} = \frac{\sum_{k=1}^N I_{ijk}}{\sum_{k=1}^N \sum_{uv} I_{uvw}}. \quad (\text{B3})$$

Under the assumption of small jitter  $\delta_k \ll 1$ , we apply the delta method and find that the pixel variance is

$$\text{Var}(I_{ij}^c) = \frac{1}{N^2 Q_B^2} \left[ \text{Var}(T_{ij}) + S_{ij}^2 \text{Var}(T_{\text{tot}}) - 2S_{ij} \text{Cov}(T_{ij}, T_{\text{tot}}) \right], \quad (\text{B4})$$

neglecting any same-shot cross-pixel covariances beyond the multiplicative term—e.g. pixel readout crosstalk or charge diffusion between pixels—we formulate the cross- and within-shot (co-)variances

$$\text{Var}(I_{ijk}) = Q_B S_{ij} + Q_B^2 S_{ij}^2 R_\delta(0), \quad (\text{B5})$$

$$\text{Cov}(I_{ijk}, I_{uvl}) = \delta_{kl} \delta_{(i,j),(u,v)} Q_B S_{ij} + Q_B^2 S_{ij} S_{uv} R_\delta(k-l). \quad (\text{B6})$$

Treating variance and covariance terms in Eq. B4 separately, we find

$$\text{Var}(T_{ij}) = \sum_{k=1}^N \text{Var}(I_{ijk}) + \sum_{k \neq l}^N \text{Cov}(I_{ijk}, I_{ijl}) \quad (\text{B7})$$

$$= N Q_B S_{ij} + Q_B^2 S_{ij}^2 \sum_{k,l=1}^N R_\delta(k-l). \quad (\text{B8})$$

The variance term for the total intensity is

$$\text{Var}(T_{\text{tot}}) = \sum_{k=1}^N \text{Var} \left( \sum_{i,j} I_{ijk} \right) + \sum_{k \neq l}^N \text{Cov} \left( \sum_{i,j} I_{ijk}, \sum_{u,v} I_{l uv} \right) \quad (\text{B9})$$

$$= \sum_{k=1}^N \left[ \sum_{i,j} \text{Var}(I_{ijk}) + \sum_{(i,j) \neq (u,v)} \text{Cov}(I_{ijk}, I_{l uv}) \right] + \sum_{k \neq l}^N \sum_{i,j} \sum_{u,v} \text{Cov}(I_{ijk}, I_{l uv}) \quad (\text{B10})$$

$$= N Q_B + \sum_{k=1}^N Q_B^2 \sum_{i,j} S_{ij}^2 R_\delta(0) + \sum_{k=1}^N Q_B^2 R_\delta(0) \left( 1 - \sum_{i,j} S_{ij}^2 \right) + \sum_{k \neq l}^N Q_B^2 R_\delta(k-l) \quad (\text{B11})$$

$$= N Q_B + Q_B^2 \sum_{k,l=1}^N R_\delta(k-l) \quad (\text{B12})$$

and for the covariance of the two we get

$$\text{Cov}(T_{ij}, T_{\text{tot}}) = \sum_{k,l=1}^N \text{Cov}(I_{ijk}, \sum_{uv} I_{l uv}) \quad (\text{B13})$$

$$= \sum_{k=1}^N \text{Cov}(I_{ijk}, \sum_{uv} I_{uvk}) + \sum_{k \neq l}^N \text{Cov}(I_{ijk}, \sum_{uv} I_{l uv}) \quad (\text{B14})$$

$$= \sum_{k=1}^N \left[ \text{Var}(I_{ijk}) + \sum_{(i,j) \neq (u,v)} \text{Cov}(I_{ijk}, I_{uvk}) \right] + \sum_{k \neq l}^N \sum_{u,v} \text{Cov}(I_{ijk}, I_{l uv}) \quad (\text{B15})$$

$$= \sum_{k=1}^N [Q_B S_{ij} + Q_B^2 S_{ij} R_\delta(0)] + \sum_{k \neq l}^N Q_B^2 S_{ij} R_\delta(k-l) \quad (\text{B16})$$

$$= N Q_B S_{ij} + Q_B^2 S_{ij} \sum_{k,l=1}^N R_\delta(k-l). \quad (\text{B17})$$

Plugging Eqs. B8, B12 and B17 into B4 yields

$$\text{Var}(I_{ij}^\circ) = \frac{S_{ij}(1-S_{ij})}{N Q_B}. \quad (\text{B18})$$

All contributions from the power density spectrum cancel out to first order. The exposure time problem is commutative; the order of summation and normalization does not affect the noise performance.

To illustrate this, we choose  $M$  to be a divisor of  $N$  and form  $K = \frac{N}{M}$  blocks of size  $M$ . For each block  $b = \{1, \dots, K\}$  one can (i) integrate and then normalize

$$T_{ij}^{(b)} = \sum_{k=(b-1)M+1}^{bM} I_{ijk}, \quad I_{ij}^{(\Sigma \rightarrow N), (b)} = \frac{T_{ij}^{(b)}}{\sum_{u,v} T_{u,v}^{(b)}} \quad (\text{B19})$$

or (ii) normalize and then integrate

$$I_{ij}^{(N \rightarrow \Sigma), (b)} = \sum_{k=(b-1)M+1}^{bM} \frac{I_{ijk}}{\sum_{u,v} I_{uvk}} \quad (\text{B20})$$

to finally combine across blocks:

$$I_{ij}^\circ = \sum_{b=1}^K I_{ij}^{(\Sigma \rightarrow N), (b)} \quad \text{or} \quad I_{ij}^\circ = \sum_{b=1}^K I_{ij}^{(N \rightarrow \Sigma), (b)}. \quad (\text{B21})$$

Since each block contributes  $\frac{S_{ij}(1-S_{ij})}{M Q_B}$  to the variance, and subdividing data into blocks does not introduce block-to-block correlations, the total variance is

$$\text{Var}(I_{ij}^\circ) = K \frac{S_{ij}(1-S_{ij})}{M Q_B} = \frac{S_{ij}(1-S_{ij})}{N Q_B}. \quad (\text{B22})$$

### Appendix C: Bias of the 0/1 Electron Counter

When repeating a 0/1 counting experiment  $K$  times, the statistical uncertainty of the sample mean estimate  $\hat{\lambda}$  improves with the number of samples taken  $\frac{\sigma_{\hat{\lambda}}}{\lambda} = \frac{1}{\sqrt{K}} \frac{\sigma_\lambda}{\lambda}$ . However, we also introduce a bias because of the nonlinearity of the logarithm. By Jensen's inequality,

$$\mathbb{E}[\hat{\lambda}] = \mathbb{E}[-\ln(\hat{P}_0)] \geq -\ln(\mathbb{E}[\hat{P}_0]) = -\ln(P_0) = \lambda. \quad (\text{C1})$$

The convex nature of  $-\ln(x)$  results in a systematic bias towards higher  $\hat{\lambda}$ . An approximation of this bias can be derived using a second-order Taylor expansion of  $f(x) = -\ln(x)$  around  $x = P_0 = e^{-\lambda}$  and applying the shifting method<sup>28</sup>:

$$\mathbb{E}[\hat{\lambda}] - \lambda = \frac{1}{2} \text{Var}(\hat{P}_0) f''(P_0) = \frac{1 - e^{-\lambda}}{2N e^{-\lambda}}. \quad (\text{C2})$$

A measurement will be significantly biased when the number of events in the counting experiment  $N$  is low. The relative error of this bias drops below  $10^{-3}$  for  $N \gtrsim 1230$  events at  $\lambda_{\text{opt}}$ .

#### Appendix D: Relative uncertainty in a diffraction feature in the presence of source noise

In this section, we will derive the relative uncertainty in a diffraction feature in the presence of source noise. Adding source noise increases the variance and thus the relative uncertainty.

We extend the single-pixel uncertainty derived in Eq. 6 of the main body of the manuscript by the multiplicative frame-to-frame source noise fluctuations described in Section III C and averaging signals belonging to the same diffraction feature over multiple pixels.

From the law of total variance we know that

$$\text{Var}(P_0) = \frac{1}{N^2} \text{Var} \left( \sum_i^N P_{0,i} \right) \quad (\text{D1})$$

$$= \frac{1}{N^2} \sum_i^N (\mathbb{E}[\text{Var}(P_{0,i}|\Lambda_i)] + \text{Var}(\mathbb{E}[P_{0,i}|\Lambda_i])), \quad (\text{D2})$$

with the Poisson rates  $\Lambda_i$  modelled as Gaussian distributed random variables with  $\mathbb{E}[\Lambda_i] = \bar{\lambda}$  and  $\text{Var}(\Lambda) = \sigma_s^2$ , and the moment-generating function  $m_k = \mathbb{E}[e^{-k\Lambda}] = e^{-k\bar{\lambda} + \frac{1}{2}k^2\sigma_s^2}$ . We find that the variance of the ratio of zero-count events is

$$\text{Var}(P_0) = \frac{1}{N} (m_1 - m_2 + m_2 - m_1^2) \quad (\text{D3})$$

$$\text{Var}(P_0) = \frac{1}{N} \left( e^{-\bar{\lambda} + \frac{1}{2}\sigma_s^2} - e^{-2\bar{\lambda} + \sigma_s^2} \right). \quad (\text{D4})$$

The first term is a counting uncertainty term that decreases with the number of events and the second term is only depending on the electron flux and the strength of the source noise. With the delta method we can write the relative uncertainty of the estimator  $\hat{\lambda} = -\ln(\hat{P}_0)$  as

$$\frac{\sigma_{\hat{\lambda}}}{\hat{\lambda}} = \frac{1}{\bar{\lambda}} \sqrt{\frac{\text{Var}(\hat{P}_0)}{\mathbb{E}[\hat{P}_0]^2}} = \frac{e^{\bar{\lambda}}}{\bar{\lambda}} \sqrt{\frac{1}{N} \left( e^{-\bar{\lambda} + \frac{1}{2}\sigma_s^2} - e^{-2\bar{\lambda} + \sigma_s^2} \right)}. \quad (\text{D5})$$

To move to the uncertainty of a diffraction feature, we define the source noise in a pixel  $(i, j)$  as a fraction of the total source noise

$$\sigma_{s,ij} = \frac{\bar{\lambda}_{ij}}{\sum_{u,v} \bar{\lambda}_{uv}} \sigma_{s,\text{tot}}. \quad (\text{D6})$$

Pixel counts follow a Poisson distribution with rate  $Y \cdot \bar{\lambda}_{ij}$ , i.e.  $N_{ij} \sim \text{Poisson}(Y \cdot \bar{\lambda}_{ij})$ , where the random variable  $Y \sim \mathcal{N}(1, \varepsilon^2)$ , common to all pixels, is a Gaussian-distributed multiplicative factor representing source noise.

For a diffraction feature over the pixel domain  $\mathcal{F}$ , across  $M$  pixels in  $N$  frames (thus  $NM$  trials), we derive the mean incident rate from the fraction of zero-events in the feature

$$P_{0,\mathcal{F}} = \frac{1}{N} \sum_k^N \frac{1}{M} \sum_{i,j}^M X_{ijk}. \quad (\text{D7})$$

The variance of this quantity is

$$\text{Var}(P_{0,\mathcal{F}}) = \frac{1}{N^2} \sum_k^N \frac{1}{M^2} \text{Var} \left( \sum_{i,j}^M X_{ijk} \right), \quad (\text{D8})$$

because the different frames are independent and different pixels in the same frame are subject to the same source noise. Further,

$$\begin{aligned} \text{Var} \left( \sum_{i,j}^M X_{ijk} \right) &= \underbrace{\sum_{i,j}^M \text{Var}(X_{ijk})}_{\approx \text{Eq. D3}} \\ &+ 2 \sum_{1 \leq (i,j) < (u,v) \leq M} \text{Cov}(X_{ijk}, X_{uvk}), \end{aligned} \quad (\text{D9})$$

with the already derived shot-noise variance for a single pixel and a covariance term between pixels that we can rewrite as

$$\text{Cov}(X_{ijk}, X_{uvk}) = \underbrace{\mathbb{E}[\text{Cov}(X_{ijk}, X_{uvk}|\Lambda_k)]}_{=0} \quad (\text{D10})$$

$$+ \text{Cov}(\mathbb{E}[X_{ijk}|\Lambda_k], \mathbb{E}[X_{uvk}|\Lambda_k]) \quad (\text{D11})$$

$$= \text{Cov}(e^{-\Lambda_k}, e^{-\Lambda_k}) \quad (\text{D12})$$

$$= \text{Var}(e^{-\Lambda_k}) = m_2 - m_1^2 \quad (\text{D12})$$

using the law of total covariances. Finally, we arrive at

$$\text{Var}(P_{0,\mathcal{F}}) = \frac{1}{N^2} \sum_k^N \left[ \frac{1}{M^2} \left( \sum_{i,j}^M (m_1 - m_1^2) \right) + M(M-1)(m_2 - m_1^2) \right] = \frac{m_1 - m_1^2}{MN} + \frac{M-1}{M} \frac{m_2 - m_1^2}{N} \quad (\text{D13})$$

$$= \frac{e^{-\bar{\lambda} + \frac{1}{2}\sigma_s^2} - e^{-2\bar{\lambda} + \sigma_s^2}}{MN} + \frac{M-1}{M} \frac{e^{-2\bar{\lambda} + 2\sigma_s^2} - e^{-2\bar{\lambda} + \sigma_s^2}}{N}. \quad (\text{D14})$$

Given  $\mathcal{F}$  contains many pixels, one can approximate  $M \approx M - 1$  and simplify further to

$$\text{Var}(P_{0,\mathcal{F}}) = \frac{e^{-\bar{\lambda} + \frac{1}{2}\sigma_s^2} - e^{-2\bar{\lambda} + \sigma_s^2}}{MN} + \frac{e^{-2\bar{\lambda} + 2\sigma_s^2} - e^{-2\bar{\lambda} + \sigma_s^2}}{N}. \quad (\text{D15})$$

The first term improves with the total number of Bernoulli trials  $MN$ , whereas the second term only improves with  $N$ , because the multiplicative jitter is common to all pixels within a given frame. Using the delta method we compute the relative uncertainty

$$\frac{\sigma_{\mathcal{F}}}{\bar{\lambda}} = \frac{e^{\bar{\lambda}}}{\bar{\lambda}} \cdot \sqrt{\text{Var}(P_{0,\mathcal{F}})}. \quad (\text{D16})$$

### Appendix E: Data management

Collecting diffraction images at a 1 kHz repetition rate produces large datasets, which require efficient storage and processing. A stack of 60,000 images stored as unsigned 16-bit integers, as saved by the camera, has a size of approximately 31.5 GB. Even if each pixel is strictly binary, most software stacks treat a boolean as the smallest addressable unit of memory—a full byte. As a result, a boolean array still uses 8 times more memory than the information-theoretic minimum. Because our detector frames are truly binary, we instead pack eight pixels in a single byte (bit-packing)<sup>29</sup>. This

transformation is lossless and reduces the memory footprint of the image stack to approximately 1.97 GB. Arithmetic operations on a packed representation are less straightforward, but the  $P_0$  counting method requires only summation. Concretely, each byte encodes eight successive pixels; we read the byte value as an unsigned integer and count the number of ones using a population count operation. For example, the pixel values

$$(0, 1, 1, 0, 1, 0, 0, 0) \mapsto 0b01101000 = (104)_{10} \quad (\text{E1})$$

are saved as a byte with decimal value 104. To sum the number of ones in those eight pixels, we apply the population count operator and obtain

$$\text{popcount}((104)_{10}) = 3. \quad (\text{E2})$$

The popcount operation is a precomputed lookup table returning the number of set bits for all integers between 0 and 255. This method does not introduce significant performance degradation.

For storage on disk we use HDF5 with chunking and in addition to bit-packing, lightweight compression filters further reduce the file size. We find that the best combination of read/write performance and file size is achieved with packed binary data in combination with a bitshuffle compression filter<sup>30</sup>. The final compression ratio versus the raw image array is 17.3. If a minimal final file size is critical, gzip compression<sup>31</sup> yields an even higher compression ratio of 23.7, but read/write performance is 15 times slower.